Battery hysteresis compensation modeling and state-of-charge estimation adaptive to time-varying ambient temperature conditions.

SHI, H., WANG, S., FERNANDEZ, C., HUANG, J., XU, W. and WANG, L.

2022

Battery hysteresis compensation modeling and state-of-charge estimation adaptive to time-varying ambient temperature conditions.

Haotian Shi[1] Shunli Wang[1] Carlos Fernandez[2] Junhan Huang[1] Wenhua Xu[1] Liping Wang[3]

[1]School of Information Engineering, Southwest University of Science and Technology, Mianyang, China

[2]School of Pharmacy and Life Sciences, Robert Gordon University, Aberdeen, UK

[3]Department of Mechanical Engineering, Tsinghua University, Beijing, China

Correspondence
Shunli Wang, School of Information Engineering, Southwest University of Science and Technology, Mianyang 621010, China.
Email: wangshunli@swust.edu.cn

Liping Wang, State Key Laboratory of Tribology and Institute of Manufacturing Engineering, Department of Mechanical Engineering, Tsinghua University, Beijing 100084, China.
Email: lpwang@mail.tsinghua.edu.cn

Funding information
China Scholarship Council, Grant/Award Number: 201908515099; National College Students Innovation and Entrepreneurship Training Program, Grant/Award Number: S202110619017; National Natural Science Foundation of China, Grant/Award Numbers: 61801407, 62173281; Southwest University of Science and Technology Student Innovation Fund Project, Grant/Award Number: CX21-018

Summary

Temperature and cell hysteretic effects are two major factors that influence the reliability and safety in long-term management of battery-integrated systems. In this paper, a hysteresis-compensated electrical characteristic model is established to track the terminal voltage of batteries with the uncertain hysteretic effect of the open-circuit voltage. Then, an autoregressive exogenous model with multi-feature coupling is employed for the identification of the parameters to make them adaptive to the uncertainties of the temperature and hysteretic effects. After that, a novel method for state-of-charge (SOC) estimation based on an adaptive moving window-square root unscented Kalman filter is constructed to avoid the filtering divergence problem caused by the negative error covariance matrix. Multiple constraints, such as Coulombic efficiency, varying ambient temperatures, and hysteresis voltage, are considered for the SOC estimation. Experimental results show that the root-mean-square error for SOC calculation can be limited to 0.0211 when the temperature varied up to 40°C and the root-mean-square error of the voltage measurement noise up to 61.9 mV. The proposed method provides an effective way for battery-integrated management of electric vehicles.

KEYWORDS
adaptive moving window-square root unscented Kalman filter, adaptive noise matching, hysteresis-compensated modeling, lithium-ion battery, state-of-charge

1 INTRODUCTION

Against the background of carbon neutrality, using batteries as the energy source to replace traditional petroleum fuels is an important measure to solve environmental problems and future energy crisis.[1] In the comparison of battery types' performance, such as lead-acid[2] and Na-Zn,[3] lithium-ion batteries have undoubtedly ranked one of the most promising energy storage systems for electric vehicles (EVs) due to their advantages, such as high cycle life, high energy density, and environmental friendliness.[4] Given the fact that thousands of series and parallel-connected high-energy-density batteries are used in the power systems of EVs to address mileage anxiety and maximum power requirements,[5] a high-performance battery management system (BMS) is critical to ensure their safe and reliable operation.

At present, researchers have made considerable efforts to reveal the complex battery modeling mechanism and state-of-charge (SOC) prediction. In the current commercial BMS, many models have been developed to provide applications for battery-integrated systems, such as lumped electrical characteristic models,[6] one-order resistor-capacitor (RC) networks,[7] fractional-order models,[8] and splice-electrochemical circuit polarization models.[9] Their model accuracy is higher in the battery type where the hysteretic effect is not obvious and in an environment where the external temperature does not change much. However, these battery modeling methods have certain limitations in the characterization of the open circuit voltage hysteresis effect, and ignore the impact of ambient temperature on the battery modeling. To effectively illustrate these issues, more needs to be known about the internal dynamic hysteretic effect of the open-circuit voltage (OCV) and the external temperature time-varying characteristics. The research of Yu et al.[10] shows that the hysteresis phenomenon of the battery makes it difficult to obtain the OCV-SOC curve accurately. Therefore, it is a valuable work to summa-rize and analyze the occurrence and coupling of the hyster-esis characteristics.

In most of the current literature, the battery equivalent circuit modeling is usually realized by ohmic impedance and resistance-capacitance links of different orders. Among them, the ohmic internal resistance is used to characterize the transient dynamic characteristics of the terminal voltage, and the resistance-capacitance link is used to characterize the gradual dynamic characteristics of the terminal voltage. However, the hysteresis effect inherent in the open circuit voltage is rarely mentioned in the literature, which contributes to the inaccuracy of battery modeling. For some battery types, such as lithium manganese oxide,[11] lithium nickel cobalt aluminum oxide,[12] and lithium nickel manganese cobalt oxide, the hysteretic effect of the OCV is not particularly obvious.[13] When modeling and analyzing the battery behavior for the above-mentioned materials, a simple and effective processing method is to take the average value of the OCV during the charging and discharging processes.[9,14] On the one hand, the error impact caused by the simplified method is not too obvious. However, it is appropriate for the online embedded application requirements of the BMS. Nevertheless, this simplified modeling approach is not suitable for lithium iron phosphate (LFP) batteries commonly used in EVs.[15,16] To assess the uncertainty of the hysteretic effect, our group tested the OCV characteristics of LFP cells in early research experiments on lumped parameter electrical characteristics modeling.[6,17] The experimental results show that the SOC value of the same OCV fluctuates between 0% and 20% during the charge and discharge state transition. Given the fact that the OCV of the LFP cell has a strong uncertainty, it is imperative to carry out targeted modeling for the OCV of LFP batteries.

In addition to the hysteresis effect of the OCV, changes in ambient temperature, especially for applications at extreme temperatures,[18] also have a large impact on the performance and state estimation of the battery model. It is worth noting that the change of ambient temperature shows strong uncertainty, which is mainly caused by the complex and changeable use environment of the battery.[19] Temperature mainly affects important parameters such as battery capacity and internal impedance.[20] Specifically, related studies have shown that the capacity varies by up to 15% under different ambient temperatures.[21-23] Although the capacity of the battery can be estimated under the current technology,[24] the hysteresis effect of the open circuit voltage and the uncertainty of the ambient temperature change are still the main reasons for the poor performance of the LFP battery. Therefore, the hysteretic voltage compensation model considering the time-varying effect of temperature is more promising.

Whereas, it is worth noting that most of these modeling strategies only estimate the model parameters at the moment. Future parameter prediction of the battery's model is more important for SOC estimation, and it seems that it cannot be obtained by the above-mentioned modeling methods. The SOC directly affects the user's choice of driving mode and future behavioral plans for the EV. Additionally, many internal state parameters, such as state-of-power,[25] remaining useful life, and state-of-energy,[26,27] are indirectly related to the with SOC in the on-board BMS of the lithium-ion battery. For instance, the joint estimation of SOC and state-of-energy can predict the available drivable distance for EVs.[28] Generally, a proper evaluation of SOC not only optimizes the management of the battery-integrated system, but, most importantly, improves the safety of EVs during operation. Because the fact that the lithium-ion battery is a nonlinear system and the uncertainty of many factors needs to be considered during the application process, it is difficult to directly derive the analytical expression for the SOC estimation.[29,30] Therefore, an estimator based on an efficient numerical calculation method is needed to achieve accurate SOC estimation. Simple SOC estimation methods such as the ampere-hour (Ah) integration[31] and the OCV[32] methods are the earliest to be applied to the BMS. Nonetheless, due to the drawbacks of open-loop estimation, these methods cannot adapt to changes in hysteresis voltage and varying ambient temperatures.

For the model-based SOC closed-loop estimation strategy, the accuracy of model parameter identification needs to be taken as the constraint condition to ensure reliable SOC estimation accuracy. Representative methods of

closed-loop estimation include the particle filter-based method proposed by Wang et al.,[33] the dual-correction extended Kalman filter proposed by Shi et al.,[34] and other adaptive estimation methods such as weighted fusion and proportional-integral.[35,36] Also, the SOC estimation accuracy is interfered with by the model, parameter identification results, and a variety of uncertain factors. For this reason, a joint SOC estimator with multi-domain coupling and multi-algorithm fusion is usually developed. For example, an adaptive asynchronous parameter identification strategy is proposed to replace the traditional online identification method under single time scale in Reference [6] Meanwhile, the deep transfer neural network with multiscale distribution adaptation is used in Reference [37] In addition, some novel algorithms have excellent performance in battery SOC prediction ability. The more typical ones include Hu et al.[38] by establishing a fractional-order equivalent circuit model and using a hybrid genetic algorithm/particle swarm optimization method for parameterization, which improves the modeling accuracy of the battery. Wang et al.[39] used a new covariance matching-electrical equivalent circuit modeling method to improve the tracking effect of terminal voltage and the estimation accuracy of SOC. In addition to the model-based SOC closed-loop estimation strategy, meta-heuristic optimization algorithms have been applied to the estimation of battery state of charge by researchers. For example, Qiao et al.[40] proposed an intelligent down-weighted firefly particle filter algorithm, and realized the real-time accurate estima-tion of the state of charge on the second-order RC equivalent circuit model. Li et al.[41] proposed an improved whale optimization algorithm to optimize the prediction process of the feedforward neural network, and further realize the accurate representation of the non-linear characteristics of the battery.

The above methods meet the online application of battery-integrated systems to a certain extent. However, in the long-term and changeable battery usage environment, the ability of these estimators to adjust online according to different load conditions and varying ambient temperatures is highly reduced. This paper establishes a hysteresis-compensated electrical characteristic model to accurately describe the battery operating mechanism. The hysteretic effect equation is iteratively coupled with the state-space equation. Then, the model-based parameters are identified online with a high-efficiency recursive least squares method under varying ambient temperatures. Finally, an adaptive moving window strategy is introduced into the square root unscented Kalman filter to avoid the filtering divergence caused by the negative error covariance matrix for SOC estimation.

The remainder of this paper is organized as follows: Section 2 describes the battery model, including the hysteresis-compensated electrical characteristic model structure, the online parameter identification method, and the adaptive moving window-square root unscented Kalman filter based SOC estimation. Section 3 comprises the experimental procedure and analysis for the parameter identification results and proposed method validation, Section 4 is the conclusion.

2 MATHEMATICAL ANALYSIS

2.1 Hysteresis-compensated RC circuit network

The hysteretic effect is one of the major factors that influence the accuracy of the internal state estimation for lithium-ion batteries. Specifically, the hysteresis effect is that there is a strong uncertainty in the OCV-SOC function during the battery charge-discharge transition. This is a description based on an experimental phenomenon, which mainly occurs at the moment when the battery transitions from the charged state to the discharged state, or from the discharged state to the charged state. For this reason, that most studies neglect to refine the characterization of hysteresis effects, a hysteresis-compensated n-order RC circuit network is established to solve the influence of hysteresis effect on model-based parameter char-acterization and state estimation. The modeling considers multiple constraints such as Coulombic efficiency and varying ambient temperatures changes to achieve the hysteresis voltage characterization. The model structure is shown in Figure 1.

In Figure 1H represents the hysteresis module, which is used to characterize the hysteresis effect of the OCV. R_0 represents the ohmic resistance, U_h represents the voltage across the hysteretic resistor, E represents the ideal voltage source, and C_b represents the cumulative capacitance. Where E and Cb together represent the OCV as U_{OC}, and

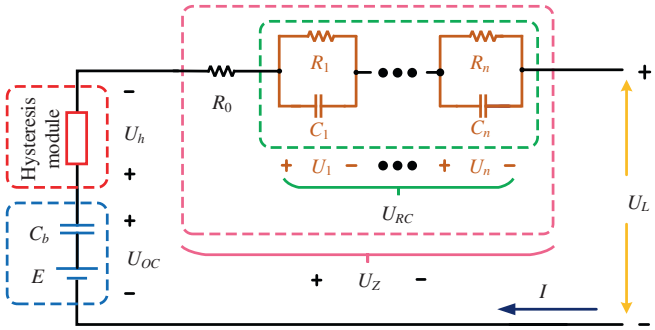

FIGURE 1 Hysteresis-compensated n-order resistor-capacitor circuit network

U_L represents the terminal voltage of the battery. R_n and C_n are the polarization resistance and capacitance for the nth RC circuit respectively. U_n represents the diffusion voltage across the nth RC circuit, and U_{RC} represents the total diffusion voltage across the nth RC circuit. U_Z represents the total voltage across the parallel circuit between R_0 and the nth-order RC circuit. I represents the charge and discharge current of the battery. The OCV based on the hysteresis-compensated n-order RC circuit comes from the optimized Nernst electrochemical empirical equation, and its feasibility and effectiveness are demonstrated in References [6, 33]. Its function value reflects the voltage optimally at both ends of the battery after no loading or shelving, as shown in Equation (1).

$$U_{OC}(S_k) = f(S_k) = m_1 + m_2 \ln(S_k) + m_3 \ln(1 - S_k) \quad (1)$$

In Equation (1), S_k represents the SOC at time k, m_1 to m_3 are the coefficients of the equation, and the value is determined by the experimental data combined with the recursive least squares (RLS) method. Combined with the principle of zero-state and zero-input response in circuit theory, the full-response equation of the diffusion voltage of this model is shown in Equation (2).

$$\begin{bmatrix} U_{1,k+1} \\ \vdots \\ U_{n,k+1} \end{bmatrix} = \begin{bmatrix} \exp[-\Delta t/R_1C_1] & \cdots & 0 \\ \vdots & \ddots & \vdots \\ 0 & \cdots & \exp[-\Delta t/R_nC_n] \end{bmatrix} \begin{bmatrix} U_{1,k} \\ \vdots \\ U_{n,k} \end{bmatrix} + \begin{bmatrix} R_1\{1 - \exp[-\Delta t/R_1C_1]\} \\ \vdots \\ R_n\{1 - \exp[-\Delta t/R_nC_n]\} \end{bmatrix} I_k \quad (2)$$

In Equation (2), Δt represents the sampling time step, I_k represents the current of the system at time step k. When the battery switches from the charging and dis-charging states to the resting state, the voltage of the ohmic resistor drops to zero instantly. With the zero-input response of the parallel RC circuit, the voltage across the circuit gradually decays to zero. At this time, the terminal voltage of the battery should theoretically be equal to the OCV value. However, it is observed that the value is not equal in actual application due to the hysteretic effect of the battery. Through the previous research and analysis in the laboratory, it is observed that the strength of the hysteretic effect has a nonlinear relationship with the degree of battery usage.[10] Therefore, this study adopts a nonlinear decay equation to model the

hysteresis effect. The mathematical expression for the calculation of the hysteretic voltage is shown in Equation (3).

$$\begin{cases} U_{h,k+1} = \exp(-|\eta I_k \varepsilon \Delta t / Q_N|) U_{h,k} \\ \qquad\qquad + [1 - \exp(-|\eta I_k \varepsilon \Delta t / Q_N|)] \operatorname{sgn}(I_k) M(S_k) \\ M(S_k) = \left[U_{OC,chg}(S_k) - U_{OC,dchg}(S_k)\right]/2 \end{cases} \quad (3)$$

In Equation (3), Q_N represents the rated battery capacity, η is the Coulombic efficiency, and ε is the hysteretic decay rate adjustment factor. $U_{OC,chg}$ and $U_{OC,dchg}$ represent the OCV during the charging and discharging phases respectively. It should be clarified that the OCV variation during the battery charging-discharge conversion can be obtained in advance through experiments, and the battery capacity and coulomb efficiency parameters can also be calibrated in advance through experiments. Therefore, using the nonlinear attenuation equation shown in Equation (3) to simulate the hysteresis effect of the battery does not increase the computational burden of modeling too much. Traditionally, the SOC of battery is defined as the ratio of the percentage of remaining capacity to the rated capacity.[42] Furthermore, the calculation of the reference value of SOC can be realized by the Coulomb counting method, which has been proved to be highly effective in calculating battery SOC.[43] The calculation of the reference value of SOC by using the Coulomb counting method is shown in Equation (4). Also, the terminal voltage output equation based on the hysteresis-compensated *n*-order RC circuit network is obtained, as shown in Equation (5).

$$S_{k+1} = S_k - I_k \cdot \eta \Delta t / Q_N \quad (4)$$

$$U_{L,k} = U_{OC,k} - U_{h,k} - \sum_{j=1}^{n} U_j - R_0 I_k \Leftarrow U_{OC,k} = f(S_k) \quad (5)$$

In Equation (5), S_{k+1} represents the SOC at time k þ 1, UL,k represents the output voltage of the model at time k, and U_j represents the voltage across the *j*th group of RC pairs.

2.2 Model-based online parameter identification

The estimation accuracy of the equivalent circuit model (ECM) is often positively correlated with the complexity of the model structure. For that reason, various factors should be weighed in practice, and then a suitable battery model should be selected. Also, the battery model in thecommercial battery-integrated system should meet the requirements of simplicity and high accuracy. As suggested by References [4, 18, 33], the first-order RC circuit network based on the hysteretic effect can characterize most of the dynamic performance of the battery while meeting the requirements of terminal voltage prediction accuracy, and the low modeling complexity makes it easy to apply in embedded systems. Therefore, this paper uses a first-order hysteresis-compensated electrical characteristic model (H-CECM) to carry out follow-up research. Using the first-order backward difference (FOBD), combined with the diffusion voltage full-response equation shown in Equation (2), the discretization equation suitable for model parameter identification is expressed as Equation (6).

$$\begin{aligned} U_{Z,k} &= U_{OC,k} - U_{L,k} - U_{h,k} = U_{1,k} + R_0 I_k \\ &= \exp(-\Delta t / R_1 C_1) U_{1,k-1} + [1 - \exp(-\Delta t / R_1 C_1)] R_1 I_{k-1} + R_0 I_k \\ &= [R_1 C_1 / (R_1 C_1 + \Delta t)] U_{Z,k-1} + [R_0 + R_1 / (R_1 C_1 + \Delta t)] I_k - [R_0 R_1 C_1 / (R_1 C_1 + \Delta t)] I_{k-1} \end{aligned} \quad (6)$$

According to the calculation results of the above equations, an autoregressive exogenous model used to identify all parameters in the H-CECM is obtained, as shown in Equation (7).

$$Y_k = \varphi_k^T \boldsymbol{\theta}_k \Leftarrow \begin{cases} \varphi_k = [U_{Z,k-1}, I_k, I_{k-1}]^T \\ \boldsymbol{\theta}_k = [a_{1,k}, b_{1,k}, b_{2,k}]^T, Y_k = [U_{Z,k}] \end{cases} \quad (7)$$

In Equation (7), θ_k and φ_k are the coefficient vector and data input vector of the autoregressive exogenous model respectively. Y_k is the output vector of the auto-regressive exogenous model. As an effective method to solve the system identification problem, RLS is used in this paper to realize the full-parameter identification of the H-CECM. According to the equation expression of the autoregressive exogenous model, combined with the experimental data input vector, the main iterative update process of the RLS algorithm is as follows:

Initialization: At the time $k=0$, initialize the coefficient matrix and error covariance matrix:

$$\begin{cases} \widehat{\boldsymbol{\theta}}_0 = E[\boldsymbol{\theta}_0] \\ \sum_0 = E\left[\left(\boldsymbol{\theta}_0 - \widehat{\boldsymbol{\theta}}_0\right)\left(\boldsymbol{\theta}_0 - \widehat{\boldsymbol{\theta}}_0\right)^T\right] \end{cases} \tag{8}$$

At the time $k=1,2,...,$ **repeat**:

1. Calculation the Kalman gain matrix

$$G_k = \sum_{k-1}\varphi_k / \left(1 + {\varphi_k}^T \sum_{k-1}\varphi_k\right) \tag{9}$$

2. Update the error covariance matrix

$$\sum_k = \sum_{k-1} - G_k {\varphi_k}^T \sum_{k-1} \tag{10}$$

3. Calculation of the coefficient vector

$$\widehat{\boldsymbol{\theta}}_k = \widehat{\boldsymbol{\theta}}_{k-1} + G_k\left(Y_k - {\varphi_k}^T \widehat{\boldsymbol{\theta}}_{k-1}\right) \tag{11}$$

4. Separation of variables to identify the parameters of the model

$$\begin{cases} R_{0,k} = b_{1,k}/a_{1,k} \\ R_{1,k} = [a_{1,k}b_{1,k} - b_{2,k}]/[a_{1,k}(a_{1,k}+1)] \\ C_{1,k} = -a_{1,k}^2 \Delta t/[a_{1,k}b_{1,k} - b_{2,k}] \end{cases} \tag{12}$$

In Equations (8) to (12), G_k is the gain matrix of the RLS algorithm at time step k. Σ_k is the error covariance matrix at time step k. $4t$ is the sampling interval. $\widehat{\theta}_k$ is the estimated value of the parameter matrix at time step k. In the iterative cycle of the above RLS algorithm, using Equation (2) and multiple sets of constant current charge-constant current discharge data, the charge and discharge OCV-SOC function of the battery can be obtained. The Coulombic efficiency η involved in the hysteresis voltage and the actual capacity of the sample battery is obtained by standard capacity calibration experiments. The value of ε is determined by the undetermined coefficient using the mathematical relationship shown in Equation (3). In this paper, the identification result of the hysteretic attenuation rate adjustment factor is ε *1/4* 1.672×10^{-3}.

2.3 | AMW-SRUKF for SOC estimation

Accurate estimation of SOC is a key issue for battery-integrated systems. When the battery operates at different ambient temperatures, it is necessary to consider multiple influencing factors such as dynamic changes in energy supply and the noise effect. Therefore, to explore a high-precision and high-robust state prediction method, it is

precision and high-robust state prediction method, it is necessary to solve the noise problem of voltage sensor measurements and current sensor measurements in the BMS first. As a solution, by modeling uncertainties of current and voltage as the process noise w_k and measurement noise v_k respectively. Then, the establishment of the state-space equation based on the H-CECM is shown in Equations (13) and (14).

$$\begin{aligned} x_{k+1} &= A_k x_k + B_k u_k + w_k \\ &= \begin{bmatrix} 1 & 0 & 0 \\ 0 & A_{RC} & 0 \\ 0 & 0 & A_{h,k} \end{bmatrix} \begin{bmatrix} S_k \\ U_{RC,k} \\ U_{h,k} \end{bmatrix} + \begin{bmatrix} -\eta \Delta t / Q_N & 0 \\ B_{RC} & 0 \\ 0 & 1 - A_{h,k} \end{bmatrix} \begin{bmatrix} I_k \\ \operatorname{sgn}(I_k) M(S_k) \end{bmatrix} + \begin{bmatrix} w_k^1 \\ w_k^2 \\ w_k^3 \end{bmatrix} \end{aligned} \tag{13}$$

$$y_k = f(x_k, u_k) + v_k = U_{OC,k} - U_{h,k} - \sum_{j=1}^{n} U_j - R_0 I_k + v_k \tag{14}$$

In Equations (13) and (14), w_k^1, w_k^2, w_k^3 and v_k are established with a zero-mean Gaussian white noise with multivariate normal distributions and covariance matrices as $w_k^1 \sim N(0, Q_1)$, $w_k^2 \sim N(0, Q_2)$, $w_k^3 \sim N(0, Q_3)$, $w_k \sim N(0, Q_k)$, $v_k \sim N(0, R_k)$, and $Q_k = \operatorname{diag}[Q_1, Q_2, Q_3]$.

From the perspective of the prediction effect, the observer based on the unscented Kalman filter (UKF)/ extended Kalman filter (EKF) method is suitable in terms of robustness. However, when the battery cell is used under highly complex conditions and there are rounding errors in numerical calculations, the UKF method cannot ensure that the covariance of its state variables is always positive. At the same time, the performance of the UKF/EKF-based observer decreases sharply or even diverges. More importantly, neither the UKF nor the EKF method can accurately track the statistical characteristics of noise, making it a problem of cumulative errors in the SOC estimation process. To reduce the computational complexity and improve the estimation accuracy of the SOC, a novel adaptive moving window-square root unscented Kalman filter (AMW-SRUKF) method based on an adaptive moving window covariance tracking strategy is proposed and applied in this work. Specifically, AWM is a strategy that can adaptively track the covariance of noise, and has excellent performance in solving the problem that traditional methods cannot accurately track the statistical characteristics of noise. The specific implementation steps are as follows:

Initialization: At the time $k = 1$, randomly generate initial particles $x_0^i (i = 1, 2, \ldots, n)$, and initialize their covariance matrix:

$$\begin{cases} P_0^i = E\left[\left(x_0^i - E(x_0^i)\right) \left(x_0^i - E(x_0^i)\right)^T \right] \\ L_0^i = \operatorname{chol}\{P_0^i\} \end{cases} \tag{15}$$

where $\operatorname{chol}\{P_0^i\}$ represents the Cholesky decomposition of the state variable error covariance P_0^i, and L_0^i represents the decomposition factor.

At the time $k = 2, 3, \ldots, N$, **repeat**:

1. Construction of a sigma point set and the corresponding weights

$$\begin{cases} x_{k-1}^i = \hat{x}_{k-1}^i, i = 0 \\ x_{k-1}^i = \hat{x}_{k-1}^i + \sqrt{(n+\lambda)} L_{k-1}^i, i = 1 \ldots n \\ x_{k-1}^i = \hat{x}_{k-1}^i - \sqrt{(n+\lambda)} L_{k-1}^i, i = n+1 \ldots 2n \end{cases} \tag{16}$$

$$\begin{cases} \omega_m^0 = \gamma / (n+\gamma) \\ \omega_c^0 = \gamma / (n+\gamma) + 1 - \alpha^2 + \beta \\ \omega_m^i = \omega_c^i = 1 / [2(n+\lambda)], i = 1 \ldots 2n \end{cases} \tag{17}$$

where n is the dimension of the state variable, N is the total number of sample sequences, γ is the scaling factor, and its value is calculated as $\gamma = \alpha^2 (n + k) - n$. α represents the spreading factor. β represents the pretest distribution factor. k is an auxiliary scale factor that satisfies $k + n \neq 0$.

2. One-step prediction of the state variable

$$\widehat{x}_{k|k-1} = \sum_{i=0}^{2n} \omega_m^i x_{k|k-1}^i \tag{18}$$

3. Perform Cholesky decomposition on the error covariance matrix of the state variable and update is decomposition factor

$$\widehat{L}_{x,k} = \mathrm{chol}\left\{ \left[\sqrt{\omega_c^{1:2n}} \left(x_{k|\mathrm{k}\text{-}1}^{1:2n} - \widehat{x}_{k|\mathrm{k}\text{-}1} \right), \sqrt{Q_k} \right] \right\} \tag{19}$$

$$L_{x,k} = \mathrm{cholupdate}\left\{ \widehat{L}_{x,k}, \sqrt{\mathrm{abs}\left(\omega_c^0\right)} \left(x_{k|k-1}^0 - \widehat{x}_{k|k-1} \right), \right. \tag{20}$$

$$\left. \mathrm{sign}(\omega_c{}^{\mathrm{O}}) \right\}$$

where $\widehat{L}_{x,k}$ and $L_{x,k}$, respectively, represent the Cholesky decomposition value and the updated value of the state variable error covariance at time step k, and the $\mathrm{cholupdate}\{*\}$ function is the update of the Cholesky decomposition.

4. One-step prediction of observation variable

$$\widehat{\mathrm{y}}_{k|k-1} = \sum_{\mathrm{i}\ 0}^{2n} \omega_m^i y_{k|k-1}^i \tag{21}$$

5. Perform a Cholesky decomposition of the error covariance matrix of the observation variable and update its decomposition factor

$$\widehat{L}_{y,k} = \mathrm{chol}\left\{ \left[\sqrt{\omega_c^{1:2n}} \left(\mathrm{y}_{k|k-1}^{1:2n} - \widehat{y}_{k|k-1} \right), \sqrt{R_k} \right] \right\} \tag{22}$$

$$L_{y,k} = \mathrm{cholupdate}\left\{ \widehat{L}_{y,k}, \sqrt{\mathrm{abs}\left(\omega_c^0\right)} \left(y_{k|k-1}^0 - \widehat{y}_{k|k-1} \right), \right.$$

$$\left. \mathrm{sign}\left(\omega_c^0\right) \right\} \tag{23}$$

where $\widehat{L}_{y,k}$ and $L_{y,k,}$ respectively, represent the Cholesky decomposition value and the updated value of the error covariance matrix of the observation variable at time step k.

6. Calculation of the error covariance matrix of the state and the observation variables

$$P_{xy,k}=\sum_{i=0}^{2n}\omega_c^i\left[x_{k|k-1}^i-\widehat{x}_{k|k-1}\right]\left[y_{k|k-1}^i-\widehat{y}_{k|k-1}\right]^T \tag{24}$$

7. Calculation of the gain matrix

$$K_k=P_{xy,k}\left(L_{y,k}L_{y,k}^T\right)^{-1} \tag{25}$$

8. Update system's state variable

$$\widehat{x}_{k|k}=\widehat{x}_{k|k-1}+K_k\left(y_k-\widehat{y}_{k|k-1}\right) \tag{26}$$

9. Update error covariance matrix of the state variable

$$L_k=\text{cholupdate}\left\{\widehat{L}_{x,k},K_kL_{y,k},-1\right\} \tag{27}$$

10. Calculate the innovation covariance function

$$E_k=\frac{1}{m}\sum_{i=k-m+1}^{k}\left(y_k-\widehat{y}_{k|k-1}\right)\left(y_k-\widehat{y}_{k|k-1}\right)_T \tag{28}$$

where, m is the adaptive window factor. E_k is the innovation covariance function at time k, and its value is used for the real-time update of system noise and observation noise.

11. Update the covariance values of process noise and measurement noise

$$\begin{cases}Q_k=K_kE_kK_k{}^T+E_k\\R_k=E_k-C_kP_kC_k{}^T\end{cases}\xrightarrow{t\to+\infty\Rightarrow P_k\to 0}\begin{cases}Q_k=K_kE_kK_k{}^T+E_k\\R_k=E_k\end{cases} \tag{29}$$

As the iteration progresses, the value of P_k will eventually tend to zero, that is when R_k tends to be equal to E_k. In the whole iterative cycle, the Cholesky update in Equations (20) and (23) replaces the time update function in the square root unscented Kalman filter (SRUKF) method ensuring the positive semi-definiteness of the error covariance matrix. The AMW-SRUKF method takes the weighted average of the variance of the innovation of the first m epochs to realize the real-time update of the current covariance noise. It is worth noting that the AMW-SRUKF method is mainly used to solve the problem that the traditional method cannot accurately track the statistical characteristics of noise and the accumulated error in the SOC estimation process. Since the whole algorithm does not introduce other unknown parameters in the iterative process, it will not increase the computational complexity of the embedded calculation of the subsequent BMS. Also, this paper uses root-mean-square error (RMSE) and mean absolute percentage error (MAPE) to describe the model and the SOC estimation effect, and the calculation method is shown in Equation (30).

$$\text{RMSE}=\sqrt{\frac{1}{N}\sum_{i=1}^{n}\left(y_i-\widehat{y}_i\right)^2},\quad \text{MAPE}=\frac{1}{N}\sum_{i=1}^{n}\frac{\left|y_i-\widehat{y}_i\right|}{y_i}\times 100\% \tag{30}$$

In Equation (30), y_i is the actual SOC value, $\widehat{y}_i$ is the estimated SOC value, and N is the total number of input samples.

2.4 Coupling principle and pseudo-code framework

The estimation accuracy of battery SOC is affected by many constraints such as Coulombic efficiency, varying ambient temperatures and hysteresis voltage. In battery-integrated system applications, the calculated SOC should satisfy all the above constraints. Following the rule and the state-space equation of H-CECM, the overall coupling principle of the presented SOC estimation using AMW-SRUKF method is shown in Figure 2.

The AMW-SRUKF method ensures the positive definite covariance of the true state variables, and realizing the adaptive tracking of the statistical characteristics of the system's noise. It should be noted that when realizing the model parameter identification and internal state estimation in the battery-integrated system, one need to pay attention to the problem of computational complexity caused by multiple constraints. Based on the modeling mechanism of H-CECM and the iterative criterion of AMW-SRUKF method, the overall SOC calculation pseudocode frame-work can be listed in Algorithm 1.

3 EXPERIMENTAL ANALYSIS

3.1 Battery specifications and experimental platform

Taking into consideration the battery usage environment, to explore the accuracy of the H-CECM under time-varying ambient temperatures, the LFP battery with rated capacity of 10 Ah and charging temperature range of 0°C to 55°C is selected as the test object for this study. The experimental device and the selected battery specifications are shown in Figure 3. The equipment of the platform mainly includes large-rate charge and discharge test equipment for power cells (CT-4016-5V100A-NTFA) and a three-layer independent temperature control high and low-temperature test chamber equipment (DGBELL BTT-331C). Also, the entire experiment charging and discharging process and data collection are controlled by the host.

3.2 Experimental procedure and model identification

In view of the complex and changeable application sce-narios of batteries, it is necessary to consider the uncertainty of temperature changes in the modeling. Specifically, the direct impact of temperature changes on battery modeling mainly includes changes in OCV-SOC function, changes in capacity, and changes in hysteresis voltage, which further affect the model parameter identi-fication results and SOC estimation accuracy. Therefore, this study focuses on the uncertainty of temperature when verifying the accuracy of the model and the accuracy of the algorithm. By setting the wide temperatures of 5C, 15C, 25C, 35C, and 45C, the temperature test chamber is used to perform the capacity correction test, the OCV-SOC test, the hysteresis voltage compensation test, the HPPC test, and the self-defined dynamic stress test (DST), and then complete the model accuracy verification under different ambient temperatures. It is worth noting that the charging temperature range of the selected lithium iron phosphate battery samples is between 0C and 55C. Therefore, considering the Coulomb efficiency and the data set requirements for OCV-SOC fitting, the temperature point distribution points of 5C, 15C, 25C, 35C, and 45C are selected. A brief description of each step of the experiment is as follows.

3.2.1 The capacity correction test

Under the control of the host, the ambient temperature of the battery sample is changed by adjusting the thermostat. Then, use the standard charging current (1C) and the standard discharging current (0.2C) to conduct a cyclic charge-discharge test on the sample battery. The actual capacity of the battery at 25°C is taken as the nominal capacity, which is 9.9826 Ah, and test the actual capacity of the battery sample at wide temperatures of 5°C, 15°C, 25°C, 35°C, and 45°C, as shown in Figure 4A. After multiple cycles of testing, the battery capacity test results and the calculation results of the Coulombic efficiency are shown in Table 1. The ratio of the actual temperature at the above temperature to the nominal capacity measured at 25°C is taken as the value of the Coulombic efficiency. By the least square fitting method, the Coulombic efficiency value at full temperature is obtained. The calculation results of the Coulombic efficiencey and the fitting curves are shown in Figure 4B.

3.2.2 The OCV-SOC test

At wide temperatures of 5°C, 15°C, 25°C, 35°C, and 45°C, using a standard discharge current (1C) to conduct a constant current discharge experiment on a full-capacity battery, and the battery sample is allowed to rest for two hours after the experiment for each ambient temperature. Then, the OCV-SOC curves under varying ambient temperatures are obtained, as shown in Figure 4A. According to the OCV characterization equation shown in Equation (1), the curve fitting function is performed based on the experimental results of OCV-SOC under varying ambient temperatures. The coefficients of the curve fitting function are shown in Table 2.

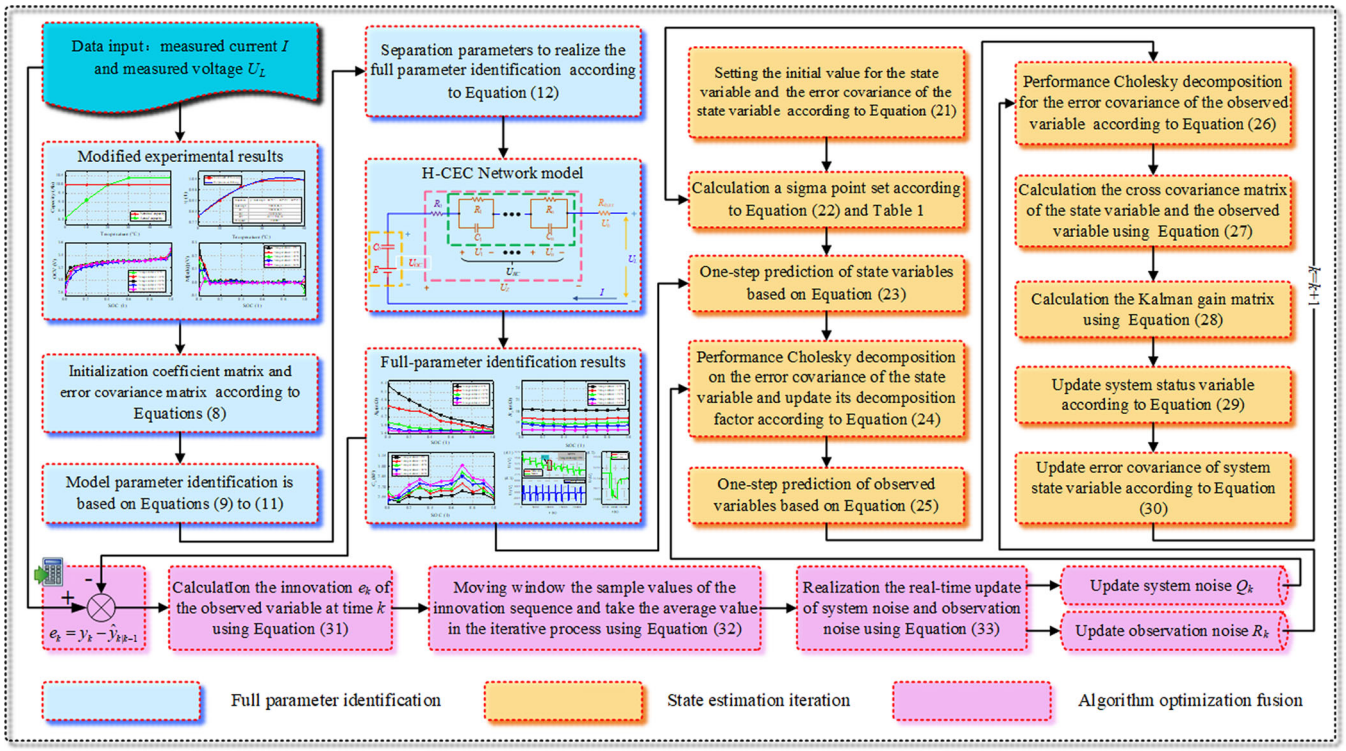

FIGURE 2 Overall coupling principle of the presented state-of-charge estimation method

3.2.3 The hysteresis voltage compensation experiment

Simultaneously with the OCV-SOC test, a constant-current charging experiment is performed on the empty battery using a standard charging current (0.2 C) at wide temperatures of 5°C, 15°C, 25°C, 35°C, and 45°C. After each temperature experiment, the battery sample rests for 2 h. Then the OCV-SOC experimental curves under varying ambient temperatures are obtained. Then, the result of $M(S_k)$ is shown in Figure 4D.

3.2.4 The HPPC test

At wide temperatures of 5°C, 15°C, 25°C, 35°C, and 45°C, the standard HPPC test is performed on the battery, the specific steps of the HPPC experiment can be found in Reference [9]. The current and voltage curves at 25°C are shown in Figure 5A-1,A-3. The Figure 5A-2,A-4 are enlarged views of a single pulse of current and voltage. In this paper, the HPPC experimental results at different temperatures are selected as the basis for model parameter identification.

3.2.5 The self-defined DST test

At wide temperatures of 5°C, 15°C, 25°C, 35°C, and 45°C, perform self-defined complex DST experiments on the battery for further verification of model fidelity and algorithm superiority at varying ambient temperatures. The experimental steps are as follows: Step 1: using a current rate of 0.5 C, a constant current discharge is applied for 60 s; Step 2: using a current rate of 0.2 C, a constant current discharge is applied for 20 s; Step 3: shelve for 10 s; Step 4: using a current rate of 0.5 C, a constant current charge is applied for 20 s; Step 5: shelve for 10 s; Step 6:1 C current constant current discharge for 120 s; Step 7: for the iterative cycle steps, Steps 1 to 6 are repeated until the end of the cycle. The DST full cycles and single-cycle experimental curves are shown in Figure 5B.

According to the above experiment, at wide temperatures of 5°C, 15°C, 25°C, 35°C, and 45°C, based on the results of HPPC experiments, the model is identified with the RLS algorithm. It should be noted that the RLS method has low computational complexity and is acceptable in terms of accuracy, and is often used in system identification. The results of the identification of each parameter are shown in Figure 6.

ALGORITHM 1 **Overall pseudo-code framework for SOC calculation**

Procedure: pseudo-code of AMW-SRUKF method based SOC estimation
  for $k = 1$
    for $i = 1$ to n
      Randomly generate initial particles x_0^i $(i = 1, 2, ..., n)$
      Initialize the covariance matrix P_0^i by Equation (15)
      Calculation of the decomposition factor L_0^i using Equation (15)
    end for
  end for
  while $k < N$
    for $k = 2$ to N
      for $i = 1$ to n
        Calculate a sigma point set and the corresponding weights by Equations (16) and (17)
        One-step prediction of the state variable using Equations (18)
        Calculate the Cholesky decomposition value $\widehat{L}_{x,k}$ by Equation (19)
        Update the decomposition factor $L_{x,k}$ by Equation (20)
        One-step prediction of observation variable using Equation (21)
        Calculate the Cholesky decomposition value $\widehat{L}_{y,k}$ by Equation (22)
        Update the decomposition factor $L_{y,k}$ by Equation (23)
        Calculate of the error covariance matrix $P_{xy,k}$ by Equation (24)
        Calculate the gain matrix K_k by Equation (25)
        Update system's state variable by Equation (26)
        Update error covariance matrix L_k by Equation (27)
        Calculate the innovation covariance function E_k by Equation (28)
        Update the covariance values of process noise and measurement noise by Equation (29)
      end for
    end for
  end while
end procedure

The experimental results in Figure 6, SOC (1) represents the actual SOC value, and its unit is normalized. The Figure 6A-1 shows the identification results of the internal ohmic resistance under varying ambient temperatures. Its value increases as the temperature decreases, and the higher the temperature, the less obvious the resistance change is during the entire SOC levels. The Figure 6A-2 shows the identification results of internal polarization resistance under varying ambient temperatures. Its value is not greatly affected by the variation of the ambient temperature. The higher the temperature, the smaller the resistance. The Figure 6A-3 shows the identification results of polarized capacitors at varying ambient temperatures. The general trend is that the higher the temperature, the larger the capacitance. The Figure 6B-1 is the comparison of the terminal voltage output under the HPPC working condition at 25°C, which is used as a model verification at a single temperature. The Figure 6B-2 shows the partial enlarged terminal voltage output curve under the HPPC working condition at 25C . It can be observed in Figure 6B-3 that at 25C , the maximum prediction error of the model terminal voltage is 0.05 V, with an accuracy of 98.81%. It shows that the parameter identification results based on the RLS algorithm have high reliability and can be used for subsequent SOC verification.

3.3 Evaluation of terminal voltage prediction accuracy

To verify the performance of the proposed H-CECM, the self-defined DST experiments are performed on selected battery sample at different temperatures. The measured and estimated results of the battery terminal voltage are shown in Figure 7. The experimental results show that the estimated terminal voltage of H-CECM matches the measured value well. It is worth noting that it can also be found from the experimental results that the estimation error of the model will increase slightly at the end of the discharge. This is mainly caused by the inevitable measurement error in the open circuit voltage experiment. Specifically, at the end of discharge, the OCV of the battery shows a rapid drop, which inevitably causes errors in its measurement. And further, the RMSE and MAPE are used to quantitatively evaluatetheperformanceofthe H-CECM,asshownin Table 3.

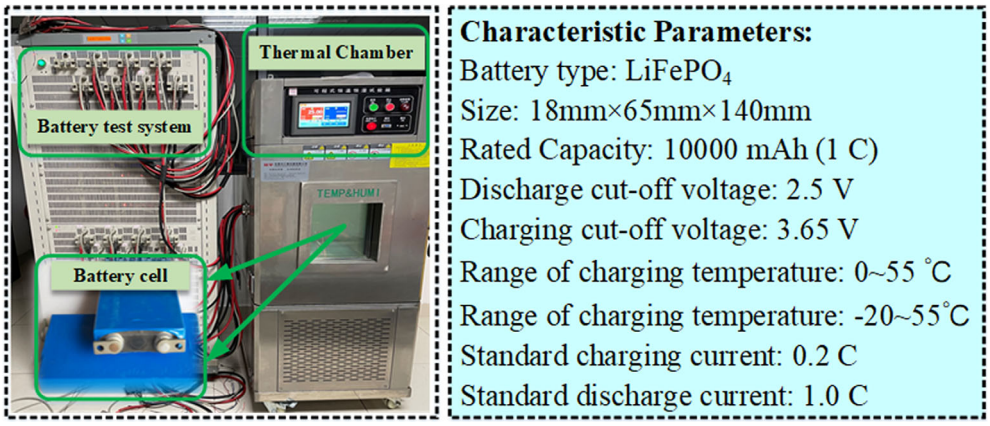

FIGURE 3 Experimental platform. Left: equipment device; Right: Battery specifications

From the evaluation results in Table 3, the MAPEs of the terminal voltage prediction based on H-CECM at wide temperatures of 5°C, 15°C, 25°C, 35°C, and 45°C, are 1.65%, 0.38%, 0.77%, 0.10%, and 0.27% respectively. Under the same temperature conditions, the RMSEs of the terminal voltage prediction based on H-CECM are 0.0559, 0.0217, 0.0312, 0.0619, and 0.0119 V respectively. Compared with the predicted results of terminal voltage at 25C and 45C in Reference [33] (the predicted RMSEs of terminal voltage at 25C and 45C are 0.0342 V and 0.0361 V), the accuracy of the model constructed in this paper is improved by 0.0030 V and 0.0242 V. This result implies that, under varying ambient temperatures, the constructed H-CECM achieves high accuracy of the terminal voltage.

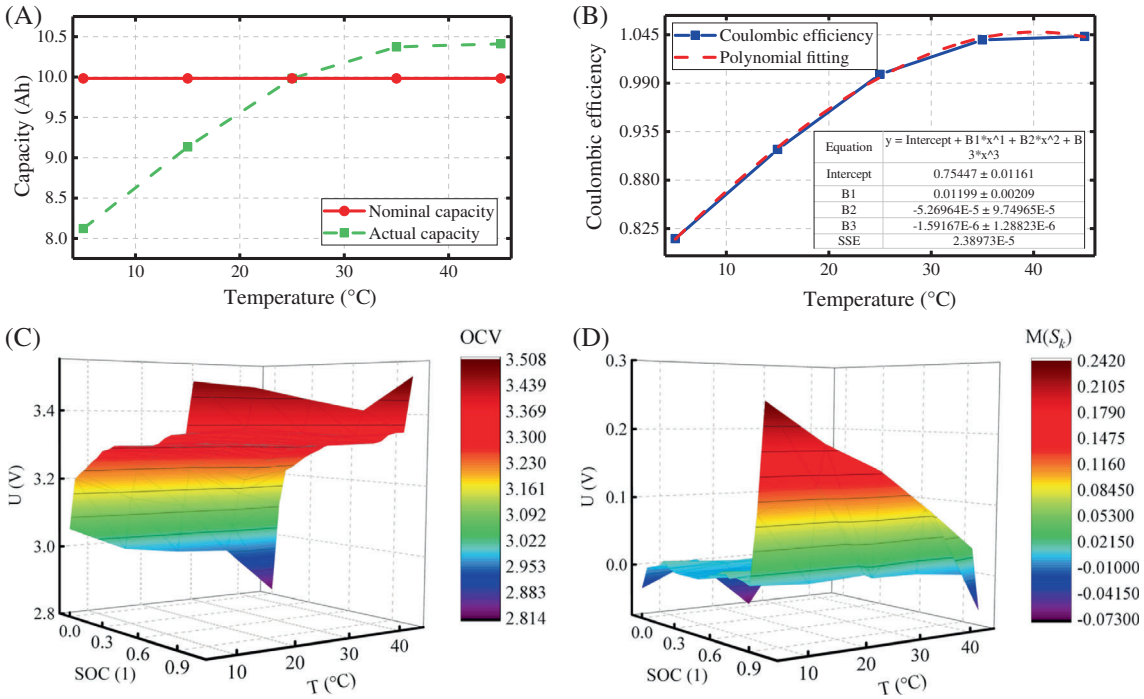

FIGURE 4 Modified experimental results under varying ambient temperatures. (A) Actual capacity; (B) Coulombic efficiency; (C) open-circuit voltage-state-of-charge curves; (D) M(S_k) results

3.4 Evaluation of SOC estimation efficiency

The actual application of lithium-ion batteries is insepa-rable from variations in ambient temperature, and an intelligent SOC estimation method must adapt to different ambient temperatures. Based on the self-defined DST complex working conditions experimental data, the estimation effects of the AMW-SRUKF algorithm under varying ambient temperatures are obtained. By comparing the estimation accuracy and convergence speed of the SRUKF and the AMW-SRUKF method using key performance metrics, the proposed algorithm's robustness and strong adaptability are verified. The estimation and error results under the self-defined DST complex conditions at wide temperatures of 5C, 15C, 25C, 35C, and 45C, are shown in Figure 8.

Temperature (°C)	5	15	25	35	45
Actual capacity(Ah)	8.1208	9.1321	9.9826	10.3729	10.4117
Nominal capacity(Ah)	9.9826	9.9826	9.9826	9.9826	9.9826
Coulombic efficiency	0.8135	0.9148	1.0000	1.0391	1.0430

TABLE 1 The Coulombic efficiency values under varying ambient temperatures

Temperature (°C)	5	15	25	35	45
m_1	3.354	3.362	3.371	3.332	3.358
m_2	0.062	0.073	0.103	0.045	0.074
m_3	−0.0024	0.0063	0.0120	−0.0065	0.0056

TABLE 2 Coefficient identification results of open-circuit voltage (OCV) at varying ambient temperatures

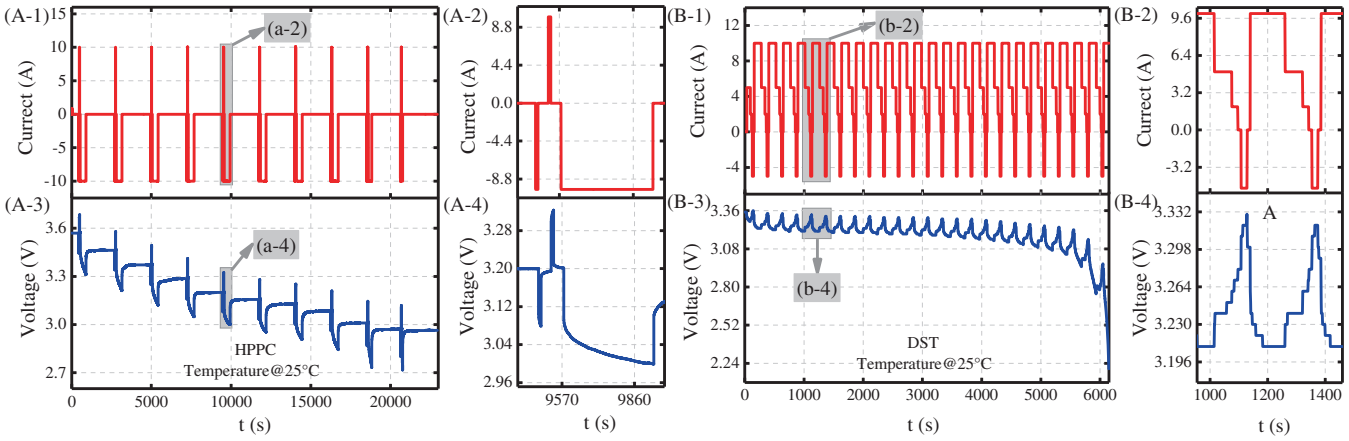

FIGURE 5 Experimental current and voltage results under HPPC and dynamic stress test (DST) working condition at 25°C.(A) Experimental results of HPPC; (B) Experimental results of DST

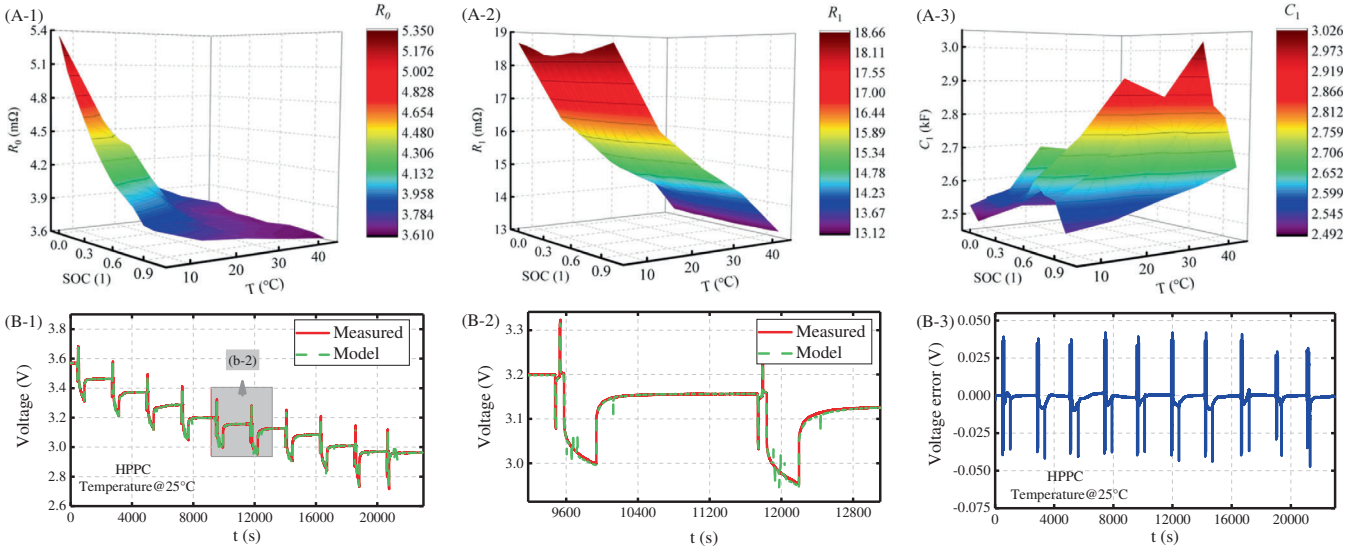

FIGURE 6 Full-parameter identification results under varying ambient temperatures. (A-1) R_0-state-of-charge (SOC) under varying ambient temperatures; (A-2) R_1-SOC under varying ambient temperatures; (A-3) C_1-SOC under varying ambient temperatures; (B-1) Terminal voltage comparison under the HPPC working condition at 25°C; (B-2) Partial enlarged under the HPPC working condition at 25°C; (B-3) Terminal voltage comparison under the HPPC working condition at 25°C

The experimental results shown in Figure 8 show that the estimator based on AMW-SRUKF method performs better than the traditional SRUKF method at different ambient temperatures. In addition, benefiting from the adaptive moving window covariance tracking strategy, the proposed method will not produce the problem of accumulated error that is not conducive to the system and the filtering divergence caused by the negative covariance in the estimation process, which makes the operation of the system more stable. Furthermore, the quantitative calculation results of RMSE and MAPE are shown in Table 5.

As can be seen from the results in Table 4, the MAPEs of the SOC observations based on AMW-SRUKF method at wide temperatures of 5°C, 15°C, 25°C, 35°C, and 45°C, are1.85%, 0.70%, 0.21%, 0.21%, and 0.33%

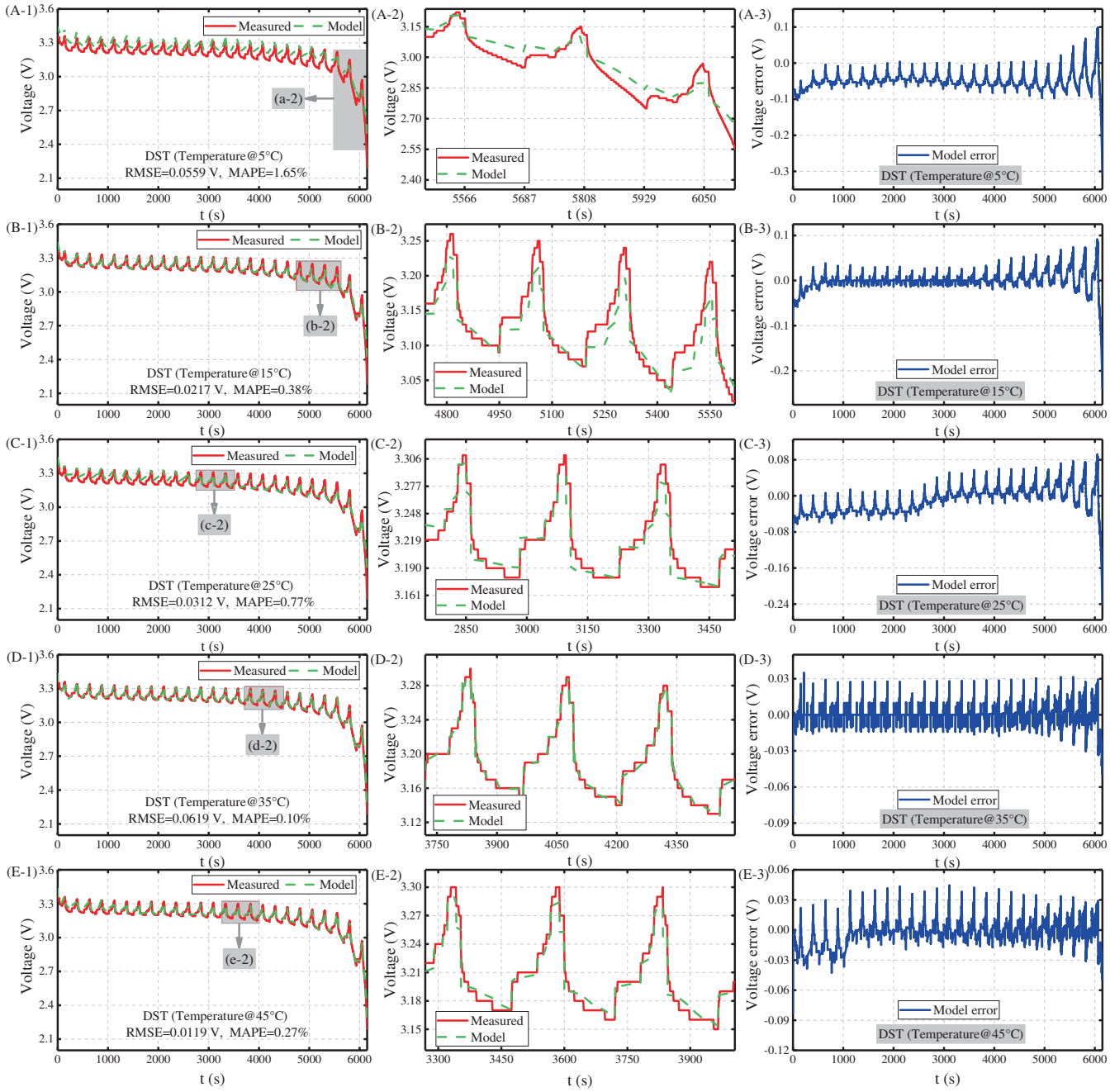

FIGURE 7 Model verification results under the self-defined DST condition. (A-1) Terminal voltage comparison at 5°C; (A-2) Partial enlarged at 5°C; (A-3) Terminal voltage comparison at 5°C; (B-1) Terminal voltage comparison at 15°C; (B-2) Partial enlarged at 15°C; (B-3) Terminal voltage comparison at 15°C; (C-1) Terminal voltage comparison at 25°C; (C-2) Partial enlarged at 25°C; (C-3) Terminal voltage comparison at 25°C; (D-1) Terminal voltage comparison at 35°C; (D-2) Partial enlarged at 35°C; (D-3) Terminal voltage comparison at 35°C; (E-1) Terminal voltage comparison at 45°C; (E-2) Partial enlarged at 45°C; (E-3) Terminal voltage comparison at 45°C

TABLE 3 Evaluation of terminal voltage prediction accuracy using root-mean-square error (RMSE) and mean absolute percentage error (MAPE)

Temperature	5°C	15°C	25°C	35°C	45°C
RMSE (V)	0.0559	0.0217	0.0312	0.0619	0.0119
MAPE (%)	1.6500	0.3800	0.7700	0.1000	0.2700

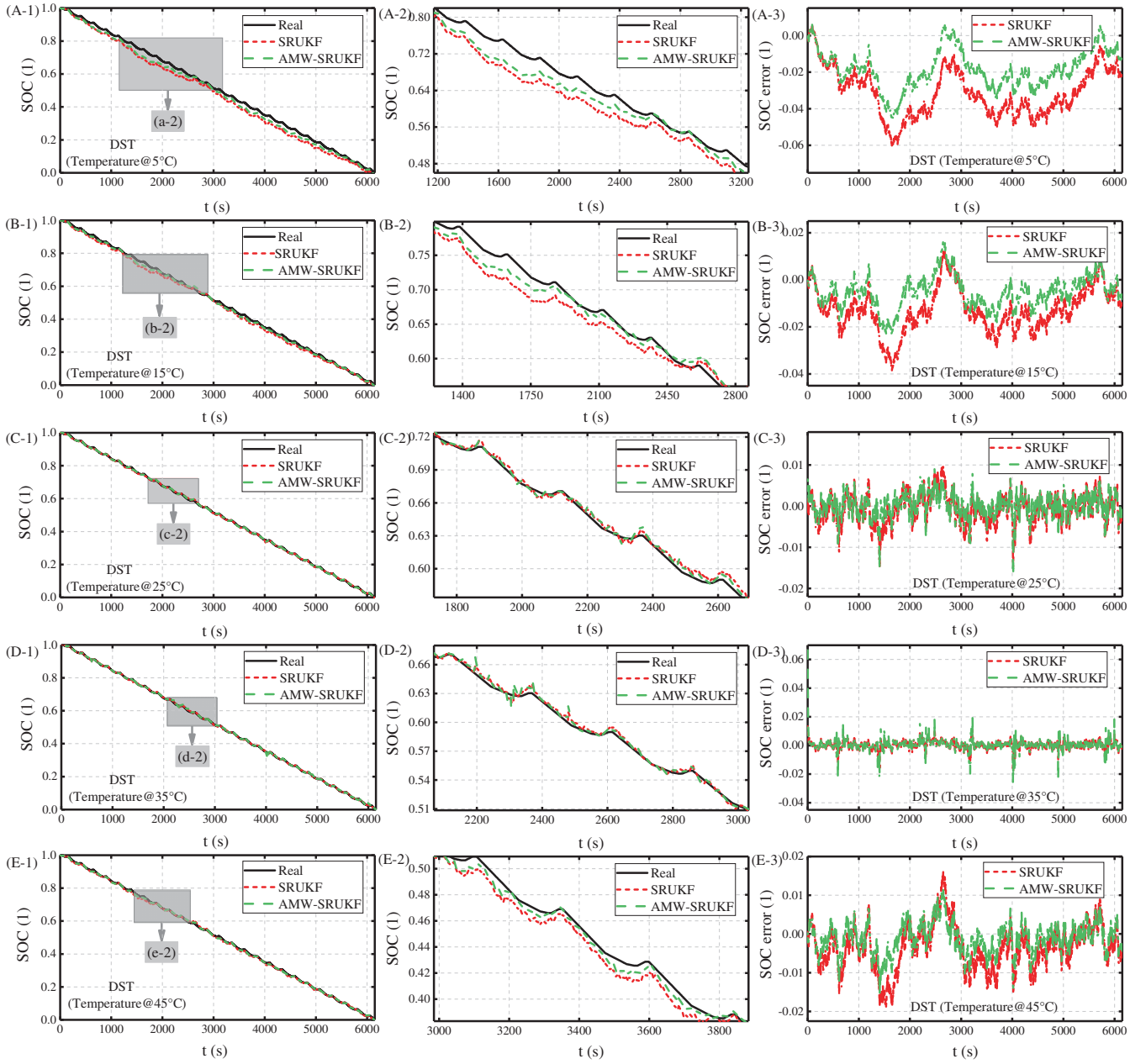

FIGURE 8 Model verification results under the custom DST condition at varying ambient temperatures. (A-1) state-of-charge (SOC) estimation at 5°C; (A-2) Partial enlarged at 5°C; (A-3) SOC error at 5°C; (B-1) SOC estimation at 15°C; (B-2) Partial enlarged at 15°C; (B-3) SOC error at 15°C; (C-1) SOC estimation at 25°C; (C-2) Partial enlarged at 25°C; (C-3) SOC error at 25°C; (D-1) SOC estimation at 35°C; (D-2) Partial enlarged at 35°C; (D-3) SOC error at 35°C; (E-1) SOC estimation at45°C; (E-2) Partial enlarged at 45°C; (E-3) SOC error at 45°C

TABLE 4 Comparison of root-mean-square error (RMSE) and mean absolute percentage error (MAPE) values under varying ambient temperatures

Temperature	5°C		15°C		25°C		35°C		45°C	
Method	SRUKF	AMW-SRUKF	SRUKF	AMW-SRUKF	SRUKF	AMW-SRUKF	SRUKF	AMW-SRUKF	SRUKF	AMW-SRUKF
RMSE (1)	0.0338	0.0211	0.0158	0.0087	0.0035	0.0028	0.0036	0.0028	0.0068	0.0042
MAPE (%)	3.1200	1.8500	1.3700	0.7000	0.2800	0.2100	0.2200	0.2100	0.5400	0.3300

respectively. The MAPEs of the SOC observations based on traditional SRUKF method at wide temperatures of 5°C, 15°C, 25°C, 35°C, and 45°C, are 3.12%, 1.37%, 0.28%, 0.22%, and 0.54% respectively. This result shows that the MAPE of SOC prediction based on the proposed method is less than that of the traditional SRUKF method over a wide temperature range. Furthermore, the RMSEs of the SOC observations based on AMW-SRUKF method at wide temperatures of 5°C, 15°C, 25°C, 35°C, and 45°C, are 0.0211, 0.0087, 0.0028, 0.0028, and 0.0042 respectively. Under the same temperature conditions, the RMSEs of the SOC observations based on SRUKF method are 0.0338, 0.0158, 0.0035, 0.0036, and 0.0068 respectively. It can be concluded that under the same temperature conditions, the RMSE of SOC prediction based on the proposed AMW-SRUKF method is smaller than that of the traditional SRUKF method. This result shows that the SOC prediction of the proposed method has a maximum RMSE of 0.0211 at the wide temperatures of 5°C, 15°C, 25°C, 35°C, and 45°C. This is 0.0089 less than the RMSE of the SOC prediction based on the UPF method in the Reference [33] (the RMSE of the SOC prediction based on the UPF method is less than 0.3 at the range of 10°C, 25°C, and 45°C). This comparison of results fully verifies the high-precision performance of the proposed AMW-SRUKF method.

4 CONCLUSIONS

High-precision modeling and accurate estimation of state-of-charge are indispensable in advanced battery management systems. This paper introduces a method for battery modeling and state-of-charge estimation in detail. First, a hysteresis-compensated resistance-capacitance circuit network model is established to achieve accurate modeling of the hysteresis effect of the battery open-circuit voltage. On this basis, an adaptive moving window square root unscented Kalman filtering algorithm is developed, and considering multiple constraints such as Coulomb efficiency, uncertainty of ambient temperature changes, and hysteresis voltage to achieve high-precision estimation of battery state-of-charge. The experimental results show that the terminal voltage RMSE and MAPE based on the hysteresis com-pensation resistor-capacitor network model are limited within 61.90 mV and 1.65%, respectively, within the tem-perature range required by the battery. Under the high-precision model parameter identification results, the RMSE and MAPE performances based on the developed state-of-charge estimation algorithm are significantly improved at various temperatures. The proposed modeling method and experimental results provide an effective way for battery-integrated management of electric vehicles or micro-grid application.

ACKNOWLEDGEMENT

The work is supported partly by the National Natural Sci-ence Foundation of China (Grant No. 62173281 and 61801407), partly by China Scholarship Council (Grant No. 201908515099), partly by Southwest University of Science and Technology Student Innovation Fund Project (Grant No. CX21-018), and partly by National College Students Innovation and Entrepreneurship Training Program (Grant No. S202110619017). Thanks to the sponsor, C.F., we would like to express our gratitude to RGU for the support.

DATA AVAILABILITY STATEMENT

The data that support the findings of this study are available from the corresponding author upon reasonablerequest.

ORCID

Haotian Shi https://orcid.org/0000-0001-8120-8310 *Shunli Wang* https://orcid.org/0000-0003-0485-8082

Junhan Huang https://orcid.org/0000-0002-8009-7863 *Wenhua Xu* https://orcid.org/0000-0002-2607-7685

REFERENCES

1. Wan BY, Tian LX, Fu M, Zhang GY. Green development growth momentum under carbon neutrality scenario. *J Clean Prod*. 2021;316:128327.
2. Jiang SD, Song ZX. A review on the state of health estimation methods of lead-acid batteries. *J Power Sources*. 2022;517: 230710.

3. Zhang ZQ, Huang GX, Tang XL, et al. Zn and Na promoted Fe catalysts for sustainable production of high-valued olefins by CO2 hydrogenation. *Fuel*. 2022;309:122105.
4. Dillon SJ, Sun K. Microstructural design considerations for Li-ion battery systems. *Curr Opin Solid State Mater Sci*. 2012;16: 153-162.
5. Katsuyama Y, Kobayashi H, Iwase K, Gambe Y, Honma I. Are redox-active organic small molecules applicable for high-voltage (>4 V) lithium-ion battery cathodes? *Adv Sci*. 2022; 9(12):2200187.
6. Shi HT, Wang SL, Wang LP, et al. On-line adaptive asynchro-nous parameter identification of lumped electrical characteristic model for vehicle lithium-ion battery considering multi-time scale effects. *J Power Sources*. 2022;515:230725.
7. Sun JL, Ma Q, Liu RH, Wang TR, Tang CY. A novel multiobjective charging optimization method of power lithium-ion batteries based on charging time and temperature rise. *Int J Energy Res*. 2019;43(13):672-7681.
8. Yu P, Wang SL, Yu CM, Jang C, Shi WH. An adaptive fractional-order extended Kalman filtering for state of charge estimation of high-capacity lithium-ion battery. *Int J Energy Res*. 2022;46(4):4869-4878.
9. Shi HT, Wang SL, Carlos F, Yu CM, Fan YC, Cao W. Improved splice-electrochemical circuit polarization modeling and optimized dynamic functional multi-innovation least square parameter identification for lithium-ion batteries. *Int J Energy Res*. 2021;45:15323-15337.
10. Yu P, Wang SL, Yu CM, Shi WH, Li BW. Study of hysteresis voltage state dependence in lithium-ion battery and a novel asymmetric hysteresis modeling. *J Energy Storage*. 2022;51: 104492.
11. Darma MSD, Lang M, Kleiner K, et al. The influence of cycling temperature and cycling rate on the phase specific degradation of a positive electrode in lithium ion batteries: a post mortem analysis. *J Power Sources*. 2016;327:714-725.
12. Raugei M, Winfield P. Prospective LCA of the production and EoL recycling of a novel type of Li-ion battery for electric vehicles. *J Clean Prod*. 2019;213:926-932.
13. Lang M, Darma MSD, Kleiner K, et al. Post mortem analysis of fatigue mechanisms in LiNi0.8Co0.15Al0.05O2-LiNi0.5Co0.2Mn0.3O2-LiMn2O4/graphite lithium ion batteries. *J Power Sources*. 2016;326:397-409.
14. Khalik Z, Donkers M, Bergveld HJ. Model simplifications and their impact on computational complexity for an electrochemistry-based battery modeling toolbox. *J Power Sources*. 2021;488:229427.
15. Zhang HM, Huang JY, Hu RH, Zhou DQ, Khan HUR, Ma CX. Echelon utilization of waste power batteries in new energy vehicles: review of Chinese policies. *J Power Sources*. 2020;206: 118178.
16. Li Y, Yang J, Song J. Design principles and energy system scale analysis technologies of new lithium-ion and aluminum-ion batteries for sustainable energy electric vehicles. *Renew Sustain Energy Rev*. 2017;71:645-651.
17. Shi HT, Wang SL, Carlos F, Yu CM, Fan YC CW. Online full-parameter identification and SOC estimation of lithium-ion battery pack based on composite electrochemical - dual circuit polarization modeling. *IOP Conf Ser: Earth Environ*. 2021;675:012192.
18. Wu LX, Pang H, Geng YF, Liu XF, Liu JH, Liu K. Low-complexity state-of-charge and anode potential prediction for lithium-ion batteries using a simplified electrochemical model-based observer under variable load condition. *Int J Energy Res*. 2022;46(9):1-15.
19. Wang SL, Fang YC, Yu CM, et al. A novel collaborative multi-scale weighting factor-adaptive Kalman filtering method for the time-varying whole-life-cycle state of charge estimation of lithium-ion batteries. *Int J Energy Res*. 2022;46(6):1-15.
20. Guo SS, Yang RX, Shen WX, Liu YS, Guo SG. DC-AC hybrid rapid heating method for lithium-ion batteries at high state of charge operated from low temperatures. *Energy*. 2022;238: 121809.
21. Du YT, Fujita K, Shironita S, et al. Capacity fade characteristics of nickel-based lithium-ion secondary battery after calendar deterioration at 80 degrees C. *J Power Sources*. 2021;501: 230005.
22. Choudhari VG, Dhoble AS, Panchal S, Fowler M, Fraser R. Numerical investigation on thermal behaviour of 5×5 cell configured battery pack using phase change material and fin structure layout. *J Energy Storage*. 2021;43:103234.
23. Ruan HJ, Sun BX, Zhang WG, Su XJ, He XT. Quantitative anal-ysis of performance decrease and fast-charging limitation for lithium-ion batteries at low temperature based on the electro-chemical model. *IEEE Trans Intell Transp Syst*. 2021;22: 640-650.
24. Wang ZP, Song CB, Zhang L, Zhao Y, Liu P, Dorrell DG. A data-driven method for battery charging capacity abnormality diagnosis in electric vehicle applications. *IEEE Trans Transp Electrif*. 2022;8(1):990-999.
25. Li WH, Fan Y, Ringbeck F, Jost D, Sauer DU. Unlocking electrochemical model-based online power prediction for lithium-ion batteries via Gaussian process regression. *Appl Energy*. 2022;306:118114.
26. Zhang SZ, Zhang XW. Joint estimation method for maximum available energy and state-of-energy of lithium-ion battery under various temperatures. *J Power Sources*. 2021;506:230132.
27. Lai X, Huang YF, Han XB, Gu HH, Zheng YJ. A novel method for state of energy estimation of lithium-ion batteries using particle filter and extended Kalman filter. *J Energy Storage*. 2021; 43:103269.
28. Shrivastava P, Soon TK, Bin Idris MYI, Mekhilef S, Adnan SBRS. Combined state of charge and state of energy estimation of lithium-ion battery using dual forgetting factor-based adaptive extended kalman filter for electric vehicle applications. *IEEE Trans Veh Technol*. 2021;70:1200-1215.
29. Shi HT, Wang SL, Carlos F, Yu CM, Li XX, Zou CY. Adaptive iterative working state prediction based on the double unscented transformation and dynamic functioning for unmanned aerial vehicle lithium-ion batteries. *Meas Control*. 2020;53:1760-1773.

30. Gao YZ, Liu KL, Zhu C, Zhang X, Zhang D. Co-estimation of state-of-charge and state-of- health for lithium-ion batteries using an enhanced electrochemical model. IEEE Trans Ind Electron. 2022;69:2684-2696.
31. Ren LC, Zhu GR, Wang JV, Luo BY, Kang JQ. Comparison of robustness of different state of charge estimation algorithms. J Power Sources. 2021;478:28767.
32. Bian XL, Wei ZG, Li WH, Pou J, Sauer DU, Liu LC. State-of-health estimation of lithium-ion batteries by fusing an OCV model and incremental capacity analysis. *IEEE Trans Power Electron*. 2022;37:2226-2236.
33. Wang YJ, Chen ZH. A framework for state-of-charge and remaining discharge time prediction using unscented particle filter. *Appl Energy*. 2020;260:114324.
34. Shi HT, Wang SL, Carlos F, Yu CM, Fan YC, Cao W. A novel dual correction extended Kalman filtering algorithm for the state of charge real-time estimation of packing lithium-ion batteries. *Int J Electrochem Sci*. 2020;15:12706-12723.
35. Lyu ZQ, Gao RJ, Li XY. A partial charging curve-based data-fusion-model method for capacity estimation of Li-ion battery. *J Power Sources*. 2021;483:229131.
36. Chi XC, Lin F, Wang YX. Disturbance and uncertainty-immune on board charging batteries with fuel cell by using equivalent load fuzzy logic estimation-based back stepping sliding-mode control. *IEEE Trans Transp Electrif*. 2021;7:249-1259.
37. Bian C, Yang SK, Miao Q. Cross-domain state-of-charge estimation of li-ion batteries based on deep transfer neural network with multiscale distribution adaptation. *IEEE Trans Transp Electrif*. 2021;7:1260-1270.
38. Hu XS, Yuan H, Zou CF, Li Z, Zhang L. Co-estimation of state-of-charge and state of health for lithium-ion batteries based on fractional-order calculus. *IEEE Trans Veh Technol*. 2018;67(11): 10319-10329.
39. Wang SL, Fang YC, Yu CM, Jin SY, Fernandez C, Stroe DI. Improved covariance matching-electrical equivalent modeling for accurate internal state characterization of packing lithium-ion batteries. Int J Energy Res. 2022;46(3):1-15.
40. Qiao JL, Wang SL, Yu CM, Yang X, Fernandez C. A novel intelligent weight decreasing firefly-particle filtering method for accurate state-of-charge estimation of lithium-ion batteries. *Int J Energy Res*. 2022;46(5):1-15.
41. Li H, Wang SL, Islam M, Bobobee ED, Zou CY, Fernandez C. A novel state of charge estimation method of lithium-ion batte-ries based on the IWOA-AdaBoost-Elman algorithm. *Int J Energy Res*. 2022;46(4):1-15.
42. Tang XP, Wang YJ, Yao K, He ZW, Gao FR. Model migration based battery power capability evaluation considering uncer-tainties of temperature and aging. *J Power Sources*. 2019;440: 227141.
43. Tang XP, Wang YJ, Zou CF, Yao K, Xia YX, Gao FR. A novel framework for Lithium-ion battery modeling considering uncertainties of temperature and aging. *Energ Conver Manage*. 2019;180:162-170.